Available online at www.sciencedirect.com
SCIENCE DIRECT®
Journal of Magnetic Resonance 176 (2005) 215–222
JMR Journal of Magnetic Resonance
www.elsevier.com/locate/jmr

Membrane gas diffusion measurements with MRI

Ziheng Zhang [a], Alexei V. Ouriadov [a], Chris Willson [b], Bruce J. Balcom [a,*]

[a] MRI Centre, Department of Physics, University of New Brunswick, Fredericton, NB, Canada E3B 5A3
[b] ElectraStor, 333 West Street, Pittsfield, MA 01201, USA

Received 20 January 2005; revised 13 June 2005
Available online 27 July 2005

Abstract

Gas transport across polymeric membranes is fundamental to many filtering and separation technologies. To elucidate transport mechanisms, and understand the behaviors of membrane materials, accurate measurement of transport properties is required. We report a new magnetic resonance imaging (MRI) methodology to measure membrane gas phase diffusion coefficients. The MRI challenges of low spin density and short gas phase relaxation times, especially for hydrogen gas, have been successfully overcome with a modified one-dimensional, single-point ramped imaging with T_1 enhancement, measurement. We have measured the diffusion coefficients of both hydrogen gas and sulfur-hexafluoride in a model polymeric membrane of potential interest as a gas separator in metal hydride batteries. The experimental apparatus is a modified one-dimensional diaphragm cell which permits measurement of the diffusion coefficient in experimental times of less than 1 min. The H_2 gas diffusion coefficient in the membrane was 0.54 ± 0.01 mm^2/s, while that of sulfur-hexafluoride was 0.14 ± 0.01 mm^2/s, at ambient conditions.

Keywords: Membrane; Diffusion; Gas phase; SPRITE; Diaphragm cell; Hydrogen; Sulfur-hexafluoride; MRI; Imaging; Magnetic resonance

1. Introduction

Gas separation by thin polymeric membranes is a dynamic and rapidly growing field [1,2]. Membrane separation processes offer a number of advantages in terms of low energy use and low capital cost, compared to rival technologies [3]. Membrane separation is commonly used for N_2 purification from air, natural gas treatment, H_2 separation from hydrocarbons, and removal of water vapor from light gas mixtures [4]. Gas separation relies on differential permeation, through the membrane, of the gas species of interest. Efficient gas separation with a polymer membrane requires that both the permeability coefficient for the desired gas, and the selectivity, should be as large as possible [5]. Differences in permeation of small molecules through membranes determine their separation properties.

The solution-diffusion model is the most widely used explanation of membrane gas phase permeation behavior. This behavior is characterized by a solubility factor, determined by the excess chemical potential, and a permeability coefficient [6,7], related to the diffusion coefficient. If the gas species is insoluble in the polymeric membrane, the membrane functions simply as a porous medium, and the solution-diffusion model can be simplified with a solubility factor set equal to one. This assumes there is no chemical potential change as gas penetrates through the membrane.

Two methods are commonly employed to characterize gas transport through membranes, (1) the 'Gurley' measurement and (2) porosity/pore size measurements. The Gurley measurement of permeability employs an oil-sealed two-cylinder system to trap a fixed volume of gas, and measures the volume of air passing through a cross-section of material per unit time. The pressure required to generate flow is provided by the weight of the inner cylinder, and the entire measurement requires

* Corresponding author. Fax: +1 506 453 4581.
E-mail address: bjb@unb.ca (B.J. Balcom).

1090-7807/$ - see front matter © 2005 Elsevier Inc. All rights reserved.
doi:10.1016/j.jmr.2005.06.009

seconds [8]. The Gurley measurement is not a satisfactory standard measurement, because the test process and measurement conditions are not closely connected to the material function.

The porosity and pore size of membrane materials are traditionally measured by capillary flow porometry, mercury porosimetry, and BET sorptometery [9,10]. While these methods characterize the void space of the membrane, which is connected to gas phase permeation, they do not directly measure mass transport through the membrane.

Direct measurement of gas diffusion coefficients is required for ready characterization and development of thin film membrane separators for use in batteries and other electrochemical systems. If such measurements are possible with a variety of membranes and gases, then such a measure has potential to become a new measurement standard.

The low spin concentrations in the gas phase are an obvious challenge to successful gas phase MRI. The resulting low SNR is a significant impediment to imaging, as is the short T_2 of gas phase species due to spin–rotation relaxation [11,12]. The short T_2 significantly impairs ones ability to employ traditional spin and gradient echo imaging methods.

SPRITE [13–15], single-point ramped imaging with T_1 enhancement, is a pure phase encode technique designed for imaging short T_2 and T_2^* spin systems, such as gas phase species [15,16]. Through the use of stepped phase encode gradients, it yields images substantially free of artifacts, but which are sensitive to T_2^* relaxation times of the gas. The centric scan strategy for SPRITE imaging removes the longitudinal steady state from the image intensity equation, and increases the inherent image SNR [17]. With a proper parameter selection, multiple FID points following each RF excitation may be acquired and utilized in the resulting image reconstruction, dramatically increasing the practical SNR [18].

2. Theory

2.1. Diaphragm-cell diffusion model

The diaphragm cell is one of the most common and best known methods for measuring liquid state diffusion coefficients [19]. Two well-stirred volumes, with a concentration difference of the species of interest, are separated by a thin porous barrier or diaphragm. The diaphragm-cell model assumes the flux across the diaphragm quickly reaches a steady-state value and that a steady-state flux is achieved even though the concentrations in the upper and lower compartments are changing with time. The pseudo steady-state changes with time as the concentration of the two reservoirs changes. The flux, j, across the diaphragm is

$$j = \left[\frac{D \cdot H}{L}\right] \cdot (C_{\text{right}} - C_{\text{left}}), \tag{1}$$

where D is the gas diffusion coefficient in the membrane. H is the partition coefficient. It has a value of 1 in our case since the gas is presumed to be insoluble in the membrane, i.e., there is no change of chemical potential between the two sides of the membrane; the gas occupies the void space in the membrane. L is the thickness of the sample film. The gas concentrations of Eq. (1) are referenced to the chamber geometry of Fig. 1.

Overall mass balance ensures that

$$\frac{\mathrm{d}}{\mathrm{d}t}(C_{\text{left}} - C_{\text{right}}) = D \cdot \beta \cdot (C_{\text{right}} - C_{\text{left}}), \tag{2}$$

where,

$$\beta = \frac{AH}{L}\left(\frac{1}{V_{\text{left}}} + \frac{1}{V_{\text{right}}}\right). \tag{3}$$

Parameter β is a sample geometry parameter, which is equal to $2.7 \times 10^6\ \mathrm{m}^{-2}$ in our experiment, with V_{right} equal to infinity, for the case of a gas volume continually refreshed by flow. At time 0, the right chamber is filled quasi instantaneously, while the left chamber remains empty. With these boundary conditions, Eq. (2), becomes

$$\frac{C_{\text{left}} - C_{\text{right}}}{C^0_{\text{left}} - C^0_{\text{right}}} = \mathrm{e}^{-\beta D t}. \tag{4}$$

In the case of gas diffusion from the right chamber to the left chamber, with the right chamber at constant concentration and the left chamber initially full of air, we may simplify Eq. (4) to

$$\frac{C(t)}{C_0} = 1 - \mathrm{e}^{-\beta D t}. \tag{5}$$

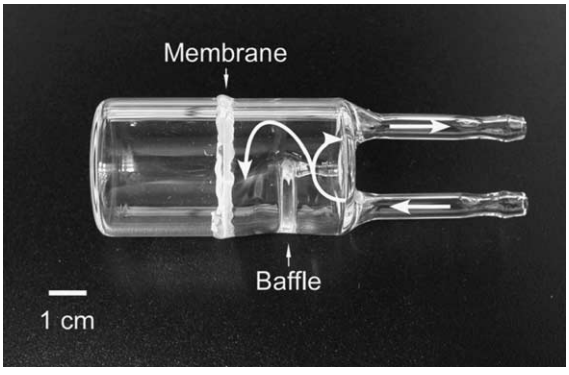

Fig. 1. Schematic of the diaphragm-cell apparatus. One glass chamber was cut into two parts and epoxied back together with the sample membrane in between. "Left" and "right" chambers are separated by the membrane. A small glass baffle deflected the input gas stream. The entire chamber was 6.2 cm in length and 3.5 cm in diameter. The film was 0.09 mm thick.

One may also consider the inverse experiment where the left chamber is full of test gas and the right chamber is maintained at zero concentration through a constant air flow. In this case, Eq. (4) simplifies to

$$\frac{C(t)}{C_0} = e^{-\beta D t}. \tag{6}$$

One-dimensional MRI images acquired with the protocol outlined below will have a local signal intensity which is directly proportional to the local test gas concentration.

2.2. Multiple FID point double half k-space

Multi-point double half k-space (DHK) SPRITE [18], featuring a centric scan, with an extended recovery time preceding each $k = 0$ RF pulse, is essentially immune to T_1-weighting. A dramatically increased data acquisition efficiency is achieved by collecting multiple FID points after each RF pulse. In this implementation, we generate a separate image for each FID point then average these images to improve SNR. Fig. 2 depicts the pulse sequence diagram for DHK SPRITE with a multiple FID point acquisition. The signal for a one-dimensional centric scan profile is proportional to

$$S = \rho_0 \cdot \exp(-t_p/T_2^*) \cdot \sin\alpha, \tag{7}$$

where ρ_0 is the nuclear spin density and α is the RF pulse flip angle. Each FID point collected following the RF excitation pulse is acquired with a unique encoding time, $t_p + (n-1)\Delta t_p$, variable t_p is the base encoding time, Δt_p is the dwell time, and n is the index of the given FID point. The FOV of any one of these images is inversely proportional to the k-space step size, Δk, which increases with each FID point detected

$$\mathrm{FOV} = \frac{1}{\Delta k} = \frac{1}{\frac{\gamma}{2\pi}\Delta G_y (t_p + (n-1)\Delta t_p)}. \tag{8}$$

The result of a SPRITE experiment, with a multiple FID point acquisition, is a set of complete images, each weighted by the T_2^* decay, and each with slightly different fields of view. Prior to image recombination for T_2^* mapping or signal averaging, all images must be corrected to a common field of view.

The chirp z-transform may be employed to transform between k-space and image space, in the case of multi-point FID data with the SPRITE technique [20]. In this strategy, we define a FOV scaling factor, Z, the ratio between the desired field of view, $\mathrm{FOV}_{\mathrm{des}}$, and the actual field of view of the image, $\mathrm{FOV}_{\mathrm{act}}$, in terms of their respective t_p value (Eq. (9))

$$Z = \frac{\mathrm{FOV}_{\mathrm{des}}}{\mathrm{FOV}_{\mathrm{act}}} = \frac{t_{P_{\mathrm{act}}}}{t_{P_{\mathrm{des}}}}. \tag{9}$$

In practice, acceptable results are observed for Z values in the range 0.75–0.9. To achieve maximum image SNR, we choose to maximize the number of FID points, 16, which corresponds to $Z = 0.75$. Theoretically, ignoring T_2^* decay, this should yield a factor of 4 SNR improvement over single FID point detection [18].

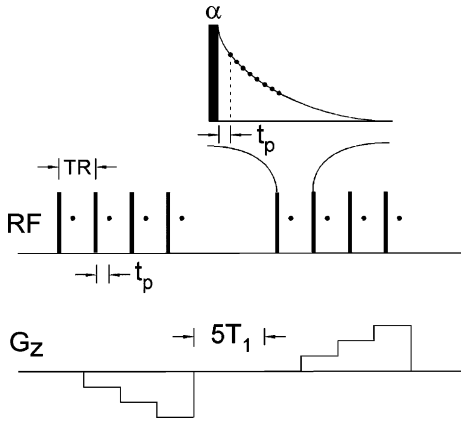

Fig. 2. MRI pulse sequence for 1D multi-point SPRITE. The RF pulses are applied at intervals of TR, with data acquisition commencing at time t_p after the RF pulse. Multiple FID points with variable t_p lead to differences in the field of views (FOV) of the individual images. A chirp z-transform (CZT) algorithm may be used to correct the images to a common field of view, during image reconstruction.

3. Results and discussion

3.1. Experimental design and data processing

A small glass diffusion cell, Fig. 1, was designed and constructed for diffusion coefficient measurement. There are two basic experiments, which may be performed with this cell, corresponding to Eqs. (5) and (6), with appropriate boundary conditions. Note that although we measure the test gas diffusion between the two chambers, this must be accompanied by counter diffusion of air between the chambers. The overall experiment will therefore also be sensitive to the counter diffusion of air through the membranes. These experiments are schematically illustrated in Fig. 3.

The experimental series of Fig. 4 illustrates the membrane gas diffusion measurement, corresponding to Eq. (5)—membrane diffusion from a well mixed constant concentration reservoir into a chamber initially at zero concentration. In this case, SF_6 is the test gas and it initially fills the right chamber without significant transmembrane diffusion, Fig. 4A. With time, Fig. 4B, gas penetrates through the membrane and finite signal is observed from the left hand chamber. The signal intensity, gas concentration in the left chamber, increases with time and is uniform and well mixed, due presumably to the very high pure gas phase diffusion coefficients

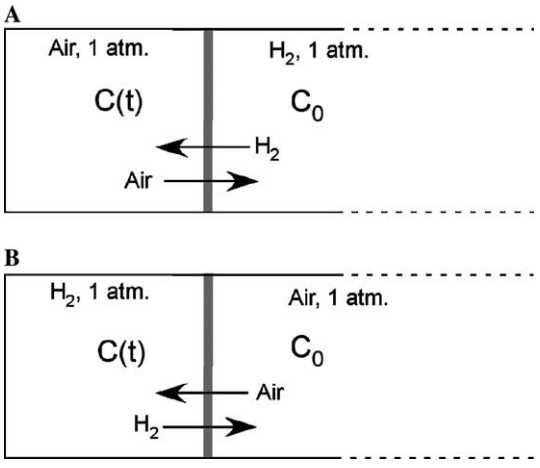

Fig. 3. Schematic diagrams illustrating the boundary conditions corresponding to diffusion into the left chamber from a constant concentration reservoir (A), and diffusion out of the left chamber into a constant concentration reservoir of zero test gas concentration (B). The thick vertical line in both (A) and (B) is the FAS-300 membrane.

and natural convention. Diffusion alone is insufficient to ensure mixing; the rms displacement during the measurement time, 0.4 s for H_2 gas, and 0.8 s for SF_6, is somewhat less than the chamber size.

The gas concentration in the left hand chamber is directly proportional to the local signal intensity. To better characterize this signal we average the image intensity between point A and B, illustrated in Fig. 4C, at each experimental time. The equilibrium concentration C_0 is determined by the average between A and B at time infinity. The ratio $C(t)/C_0$, Eq. (5), at any experimental time is given by the normalized, averaged image intensities.

3.2. Diaphragm-cell assumptions

The diaphragm-cell model makes several critical assumptions in analyzing $C(t)/C_0$, which we must revisit. The test polymer film should be homogeneous; the diffusion coefficient is assumed constant resulting in a

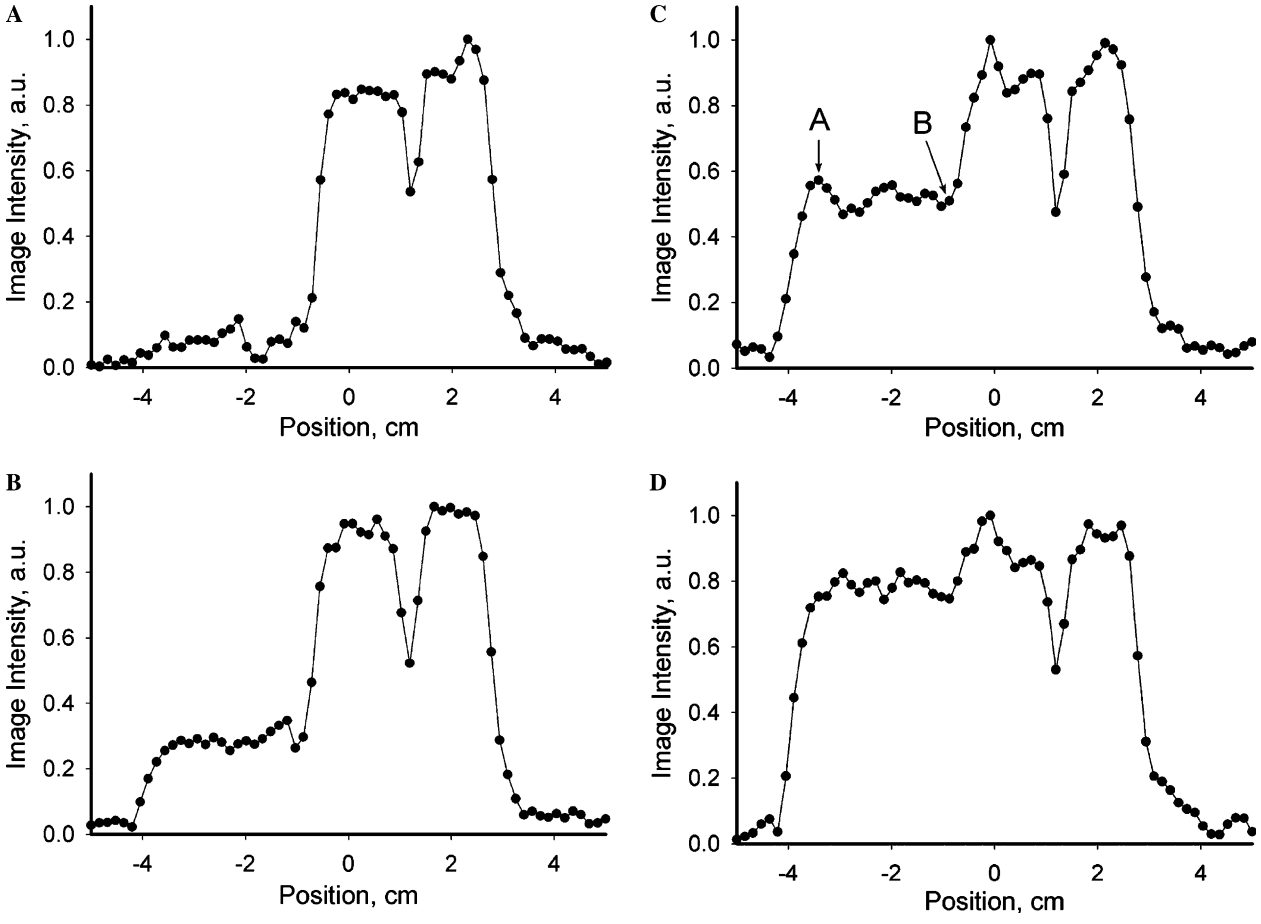

Fig. 4. Discrete one-dimension profiles illustrating the diffusion process (sulfur-hexafluoride). (A) MRI image shows gas concentration immediately following test gas flow into the right chamber, but before significant membrane diffusion has occurred. (B) MRI image 4.8 s later. Gas is now beginning to fill the left chamber. Note the quite uniform image intensity. (C) MRI image 13 s after commencement of gas flow. The uniform image intensity between point A and B is averaged at each experimental time to provide a measure of the instantaneous gas concentration. (D) MRI image 34 s after commencement of gas flow. Note the intensity dip in the right side of the image due to the baffle.

classical Fickian time dependence of the diffusion process; both instantaneous and steady interfacial polymer equilibriums are required; and the mass transfer direction should be perpendicular to the polymer film [21,22]. All are quite reasonable assumptions for the materials and diffusion cell employed.

A gas flow of speed 40 ml/s into the right hand chamber with a chamber volume of 18 ml means the gas flux will fill this volume within 0.45 s. We assumed that filling the right chamber is quasi instantaneous. The input gas stream will collide with the glass baffle and generate swirling eddies in the right side chamber. These eddies help maintain a homogeneous gas concentration in the right hand chamber.

We also assume that gas flow across the membrane is not driven by pressure differences between the two chambers. According to Bernoulli's law [23], ignoring viscosity, the flow speed and the gauge pressure are related by

$$P = \rho \cdot v^2/2. \tag{10}$$

Here, ρ is the density of gas at room temperature, 0.0899 g/L for hydrogen gas and 6.17 g/L for SF_6. The pressure potential to drive the flow into the reservoir is ~6.6 Pa for hydrogen and 450 Pa for SF_6. These pressures are negligible compared to the 1 atm (1.01×10^5 Pa) pressure in each chamber at equilibrium. The pressure in both chambers will rapidly balance due to mass transport and we consider the entire process to be purely diffusive.

3.3. Diaphragm-cell diffusion results

At 1 atm and ambient temperature, the spin–lattice relaxation times were measured to be: $T_1 = 1.0 \pm 0.2$ ms for H_2 and $T_1 = 1.4 \pm 0.1$ ms for SF_6. Different gas concentrations and more importantly in this context, local oxygen concentration, yield different spin lattice relaxation times [11,12]. The DHK technique, as a centric scanning strategy, is essentially immune to image intensity variation due to variable T_1. This characteristic of the DHK approach permits direct determination of the test gas concentration. The only effect caused by variation in T_1 is a potential blurring of the image. However, as depicted in Fig. 4, no significant blurring was observed.

An increasing oxygen partial pressure will also alter the gas phase T_2 relaxation time with potential therefore to alter the T_2^* time constant. However, the T_2^* time is substantially reduced from the T_2 value due to the static field inhomogeneity in our magnet—which is never shimmed for measurements of this type. The H_2 T_2 time constant changes from 0.9 ± 0.2 ms at 1 atm and ambient temperature, to 0.65 ± 0.2 ms with a 50% partial pressure of air. The T_2^* value however is essentially unchanged at 260 μs. Similar result are obtained for SF_6 with a T_2^* value of 850 μs. Once more, the images generated are density weighted due to a short t_p, $t_p \ll T_2^*$, and a T_2^* which is dominated by local magnetic field inhomogeneity.

For hydrogen gas, which has the second highest self-diffusion coefficient at standard temperature and pressure (helium is highest), standard imaging techniques, such as frequency encoding spin echo methods, will not generate ideal density weighted images. For example, in the case of a conventional spin echo measurement with an echo time of 2 ms and FOV of 10 cm, the signal intensity at the centre of k-space will be attenuated by more than 50% due to self-diffusion. As a pure phase encoding centric scan technique, the DHK technique is immune to signal intensity attenuation caused by self-diffusion through imaging field gradients, since at the k-space centre the diffusion contrast is zero [24].

The imaging experiments outlined in this paper permit a direct quantitative determination of the membrane gas diffusion coefficient. As an imaging measurement, however, they also provide a direct experimental check on the boundary conditions for Eqs. (5) and (6). For example, time lapse MRI measurements of H_2 and SF_6 diffusion, corresponding to Eq. (6) boundary conditions, reveal that the test gas concentration in the right hand chamber is not zero.

We hypothesize that the presence of the baffle, which is necessary to prevent the input gas striking the membrane directly, prevents the most efficient sweep of the test gas from the zero concentration chamber in experiments corresponding to Eq. (6) boundary conditions. Air flow into the right chamber is not sufficient to prevent a gas boundary layer developing near the membrane interface. The boundary conditions appropriate to Eq. (6) are not fulfilled and this geometry has not been pursued. By contrast, time lapse MRI measurements of experiments utilizing Eq. (5) boundary conditions show that the boundary conditions are well satisfied. The test gas concentrations in each chamber are uniform and well mixed with $C_{\text{right}} = C_0$ and $C_{\text{left}} = 0$ at time 0.

Fitting the experimental ratio $C(t)/C_0$ to Eq. (5) determines the diffusion coefficients of the test gases, Fig. 5. The results of repetitive measurements of H_2 and SF_6 diffusion are reported in Table 1. The diffusion measurements for SF_6 are very reproducible, with an uncertainty between measurements no greater than the uncertainty of fitting individual experiments. In the case of an H_2 experiment, this is no longer true. The H_2 experiment is more challenging due to the rapidity of the diffusion. The uncertainty is greater between individual experiments than the uncertainty derived from data fitting. In both the H_2 and SF_6 cases, we report the uncertainty of the average values, Table 1, through a simple determination of the standard error rounded to the least significant digit.

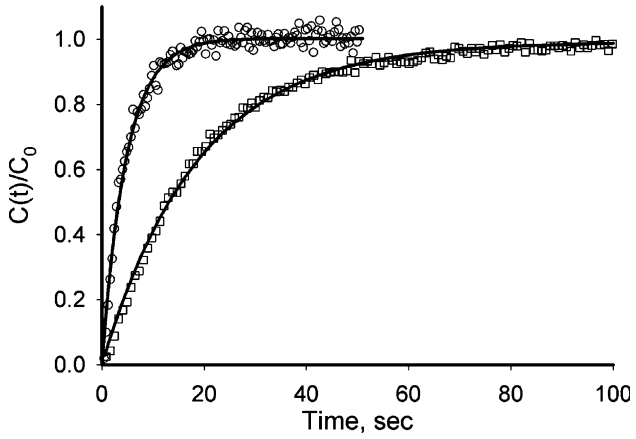

Fig. 5. The diaphragm-cell result for H_2 and SF_6 diffusion into the left chamber. Experimental data are fit to Eq. (5), a single exponential function. The symbols (○) represent the ratio, $C(t)/C_0$, for a hydrogen gas experiment. The average diffusion coefficient was 0.54 ± 0.01 mm^2/s. Symbols (□) correspond to the same experiment and apparatus, but for sulfur-hexafluoride gas diffusion. The average diffusion coefficient was 0.14 ± 0.01 mm^2/s.

Table 1

Experiment number and average result	Diffusion coefficient (mm^2/s)[a]	
	Hydrogen	Sulfur-hexafluoride
1	0.53	0.14
2	0.57	0.13
3	0.56	0.14
4	0.50	0.14
Average	0.54 ± 0.03	0.14 ± 0.01

[a] The fitting uncertainty was typically ± 0.01 mm^2/s.

3.4. Permeability and tortuosity

In membrane technology, the most direct and important parameter is the permeability of the test membrane. The permeability, P, is determined by the product of the diffusion coefficient and the solubility, normalized by the membrane thickness [19]

$$P = \frac{D \cdot H}{L}. \tag{11}$$

As mentioned previously, we assume our gases are not soluble in the membrane and therefore $H = 1$. The permeability of the test membrane, according to Eq. (11), was 6.00 ± 0.11 mm/s for H_2, and 1.56 ± 0.11 mm/s for SF_6 at ambient conditions.

The tortuosity is a structural characteristic of the porous medium, which describes the sinuosity and interconnectedness of the pore space as it affects macroscopic transport [25]. The effective diffusion coefficient can be defined as [19,25]

$$D_{\text{eff}} = \left(\frac{\delta}{\tau}\right) \cdot D_0 = \frac{D_0}{\tau_{\text{eff}}}, \tag{12}$$

where, D_0 is the pure gas phase self-diffusion coefficient, δ is the void fraction, and τ is the tortuosity, while τ_{eff} is the effective tortuosity. The equation essentially means that the diffusion coefficient in the porous medium is equal to the pure gas phase diffusion coefficient reduced by a geometric factor; other definitions of the tortuosity also exist in the literature [19].

The pure bulk gas self-diffusion coefficients of hydrogen and sulfur-hexafluoride were measured using the pulse field gradient (PFG) method [26]. The results, at temperature, 20 °C, and one atmosphere were 83 mm^2/s for hydrogen gas, and 11 mm^2/s for sulfur-hexafluoride, which agrees very well with the literature value of 9.6 mm^2/s, at 17 °C [27].

The effective tortuosity, from Eq. (12), is therefore 150 for hydrogen and 80 for sulfur-hexafluoride. The tortuosity effect is about two times greater for hydrogen gas than that for sulfur-hexafluoride. Somewhat surprisingly, the membrane has a greater effect on the mass

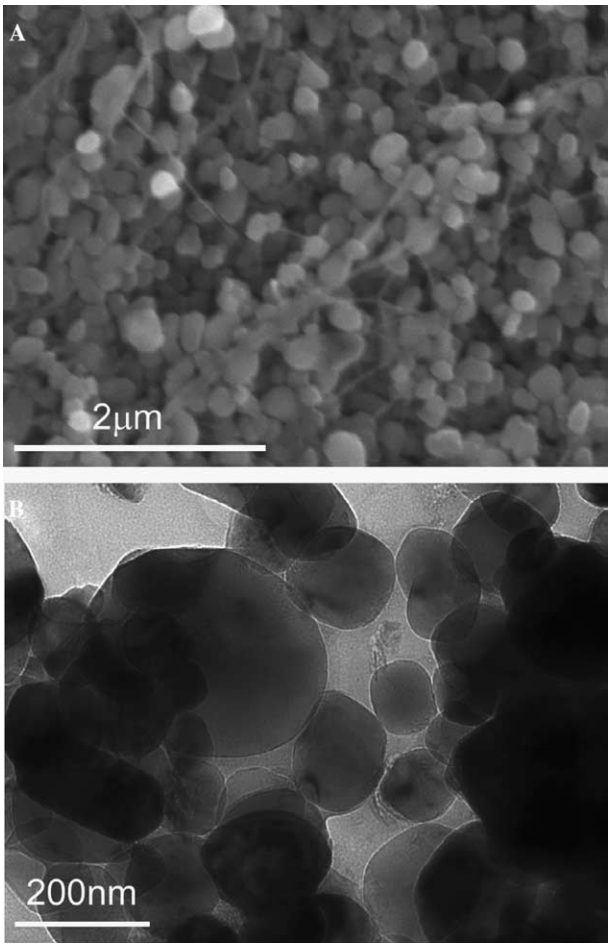

Fig. 6. SEM and TEM images of the FAS-300 membrane. (A) SEM image. The sample is composed of submicron particles with thin filaments visible which are less than 0.1 μm thick, but more than 1 μm in length. (B) TEM image. The particles range in size from 0.1 to 0.3 μm in diameter. The ultra-thin cross-section visualized is ~70 nm in thickness.

transport of hydrogen than it does for sulfur-hexafluoride. The molecular diameter of hydrogen is 2.34×10^{-10} m [23], while that of sulfur-hexafluoride is 5.02×10^{-10} m [28]. The nominal pore size range, from Fig. 6, is on the order of 0.1 μm which is large compared to the molecular diameters. Both molecules are thus in the same Knudsen diffusion range. We interpret the higher tortuosity of hydrogen as a measure of the fact the smaller hydrogen molecule may penetrate into regions of the pore pace inaccessible to the larger sulfur-hexafluoride. Alternatively, there may be a specific interaction between the membrane and hydrogen gas which retards the mass transport. Regardless, the results of these measurements provide a direct measure of the relative transport properties of the membrane.

SEM and TEM were used to examine the membrane structure of the FAS-300 film. The resulting images are shown in Fig. 6. The membrane consists of particles typically ranging from 0.1 to 0.3 μm in diameter. There are also thin filaments visible which are less than 0.1 μm thick, and more than 1 μm in length. From the TEM image, the pore space ranges from less then 0.1 to 0.4 μm in diameter, due to the loose packing of the constituent particles of the sample.

4. Conclusion

This paper describes a new diffusion measurement which combines the diaphragm-cell diffusion measurement with MRI methods. Multi-point DHK SPRITE permits rapid gas phase imaging in samples with short relaxation times. The acquisition times for each 1D profile are 0.4 s for hydrogen gas and 0.8 s for SF_6, respectively. The corresponding diffusion coefficients are 0.54 ± 0.01 mm^2/s for hydrogen and 0.14 ± 0.01 mm^2/s for sulfur-hexafluoride.

The tortuosity difference, and thereby permeability difference, between H_2 and SF_6, is significant because the water saturated FAS membrane is intended to be a putative gas separator membrane. While a simple MRI measurement, the diaphragm cell combined with MRI is a measurement with significant scope for improvement and extension.

These mass transport measurements are directly connected to the membrane function. The potential therefore exists for the new methodology to become a standard measurement for membrane characterization.

5. Experimental

5.1. Apparatus

A Pyrex glass cylinder, 3.5 cm in diameter and 6.2 cm in total length (Fig. 2), was cut in two then reconnected with a 5 min epoxy (Lepage). The sample film, FAS-300 (Advanced Membrane Systems, VA, USA), was well sealed in between the two cylinders. The film was 0.09 mm thick. A small glass baffle was added to the cell to prevent the input gas flux directly striking the film. The left side chamber was 3 cm in length.

5.2. MRI details

The 1D DHK SPRITE experiment was implemented on a Nalorac (Martinex, CA) 2.4T 32 i.d. horizontal bore superconducting magnet with a water cooled 7.5 cm i.d. gradient set (maximum gradient strength 100 G/cm) driven by a Techron (Elkhart, IN) 8710 amplifier, which provided 17 G/cm gradients for hydrogen experiments and 13 G/cm gradients for sulfur-hexafluoride experiments. The RF probe was a ^{1}H free 32 element quadrature birdcage coil (Morris Instruments, Ottawa) for ^{1}H imaging. A homebuilt quadrature birdcage probe was employed for ^{19}F imaging. Both probes were driven by a 2 kW AMT (Brea, CA) 3445 RF amplifier. The imaging console was a Tecmag (Houston, TX) Apollo in both cases.

Standard inversion recovery and CPMG methods were employed to measure spin–lattice relaxation and spin–spin relaxation times. Bulk T_2^*s were measured by exponential fitting to the free induction decay.

The repetition time, TR, was set to 0.6 ms for both gases and the base encoding time, t_p, was set to 46 μs for hydrogen and 52 μs for sulfur-hexafluoride. Dwell times were selected as 1 and 2 μs, respectively, for hydrogen and sulfur-hexafluoride. To fix both FOVs at 10 cm, the gradient increment, ΔG, was set to 0.53 G/cm for H_2 and 0.42 G/cm for SF_6. The rf pulse width for both gases was set to 6 μs with a flip angle α of 49° for hydrogen and 19° for sulfur-hexafluoride. Eight signal averages were collected for hydrogen gas imaging and 16 for sulfur-hexafluoride gas imaging, with 16 FID points collected for each. The image SNR increased by a factor of 2.8, instead of the theoretical limit of 4, due to the collection of multiple FID points. The image acquisition time for an H_2 image was 0.4 s, while it was 0.8 s for an SF_6 image.

Acknowledgments

B.J.B. thanks NSERC of Canada for operating and equipment grants. B.J.B also thanks the Canada Chairs program for a Research Chair in MRI of Materials (2002–2009).The MRI Centre is supported through an NSERC Major Facilities Access award. We thank R.P. MacGregor for his assistance with the experiments and Dr. B. MacMillan, M. Halse, J. Rioux, and Y. Cheng for helpful discussions. We thank B. Malcolm for fabricating the diaphragm cell as well as Dr. D.C.

Hall, Dr. L. Weaver, and S. Belfry for their assistance with the SEM and TEM measurements, and C. Poirier for the pressure distribution simulation.

References

[1] S.A. Stern, Polymers for gas separation: the next decade, J. Membr. Sci. 94 (1994) 1.
[2] G. Maier, Gas separation with polymer membranes, Angew. Chem. Int. Ed. 37 (1998) 2960.
[3] P. Pandey, R.S. Chauhan, Membranes for gas separation, Prog. Polym. Sci. 26 (2001) 853–893.
[4] R. Rautenbach, R. Albrecht, Membrane Processes, John Wiley & Sons Ltd., New York, 1989.
[5] Z. Xu, C. Dannenberg, J. Springer, S. Banerjee, G. Maier, Novel poly(arylene ether) as membranes for gas separation, J. Membr. Sci. 205 (2002) 23–31.
[6] J.G. Wijmans, R.W. Baker, The solution-diffusion model: a review, J. Membr. Sci. 107 (1995) 1–21.
[7] Y. Tsujita, Gas sorption and permeation of glassy polymers with microvoids, Prog. Polym. Sci. 28 (2003) 1377–1401.
[8] J.W. Walkinshaw, G.A Hagerty, Analysis of Gurley-type air permeability measurement and the use of electronic flow sensors, TAPPI J. 75 (1992) 181–185.
[9] Gupta, Vibhor, A.K. Jena, Advances in Filtration and Separation Technology, American Filtration and Separation Society, Northport, Alabama, 1999, p. 833.
[10] A.K. Jena, K.M. Gupta, In-plane compression porometry of battery separators, J. Power Sources 80 (1999) 46–52.
[11] R.L. Armstrong, Longitudinal nuclear spin relaxation time measurements in molecular gases, in: M.M. Pintar (Ed.), NMR 13 Basic Principles and Progress, 13, Springer-Verlag, Heidelberg, 1975, p. 77.
[12] R.L. Armstrong, Nuclear magnetic relaxation effects in polyatomic gases, Magn. Reson. Rev. 12 (1987) 91.
[13] B.J. Balcom, SPRITE imaging of short relaxation time nuclei, in: Spatially Resolved Magnetic Resonance, Wiley-VCH, Toronto, 1998, pp. 75–86.
[14] S.D. Beyea, B.J. Balcom, P.J. Prado, A.R. Cross, C.B. Kennedy, R.L. Armstrong, T.W. Bremner, Relaxation time mapping of short T_2^* nuclei with single-point imaging methods, J. Magn. Reson. 135 (1998) 156–164.
[15] P.J. Prado, B.J. Balcom, I.V. Mastikhin, A.R. Cross, R.L. Armstrong, A. Logan, Magnetic resonance imaging of gases: a single-point ramped imaging with T_1 enhancement (SPRITE) study, J. Magn. Reson. 137 (1999) 324–332.
[16] B. Newling, C.C. Poirier, Y. Zhi, J.A. Rioux, A.J. Coristine, D. Roach, B.J. Balcom, Velocity imaging of highly turbulent gas flow, Phys. Rev. Lett. 93 (2004) 154503.
[17] I.V. Mastikhin, H. Mullally, B. MacMillan, B.J. Balcom, Water content profiles with a 1D centric SPRITE acquisition, J. Magn. Reson. 156 (2002) 122–130.
[18] M. Halse, J. Rioux, S. Romanzetti, J. Kaffanke, B. MacMillan, I. Mastikhin, N.J. Shah, E. Aubanel, B.J. Balcom, Centric scan SPRITE magnetic resonance imaging: optimization of SNR, resolution, and relaxation time mapping, J. Magn. Reson. 169 (2004) 102–117.
[19] E.L. Cussler, Diffusion: Mass Transfer in Fluid System, Cambridge University Press, Cambridge, 1984.
[20] L.R. Rabiner, R.W. Schafer, C.M. Rader, The Chirp z-transform algorithm and its application, Bell Syst. Tech. J. (1969) 1249–1292.
[21] J. Crank, G.S. Park, Diffusion in Polymers, Academic Press, London, New York, 1968.
[22] H.S. Carslaw, J.C. Jaeger, Conduction of Heat in Solids, second ed., Oxford University Press, New York, 1959.
[23] R.C. Weast, Handbook of Chemistry and Physics, fifty-seventh ed., CRC Press, Cleveland, Ohio, 1976–1977.
[24] S. Gravina, D.G. Cory, Sensitivity and resolution of contrast-time imaging, J. Magn. Reson. B 104 (1994) 53.
[25] A. Tuli, J.W. Hopmans, Effect of degree of fluid saturation on transport coefficients in disturbed soils, Eur. J. Soil Sci. 55 (2004) 147–164.
[26] D.L. Bihan, Diffusion and Perfusion Magnetic Resonance Imaging, Raven Press, New York, 1995.
[27] B.P. Nikolskiy, Chemical equilibrium and kinetic properties of solutions, electrode processes, Handbook of Chemist, vol. 3, second ed., Khimiya, Moscow-Leningrad, 1965–1968 (Russian).
[28] J. Koresh, A. Soffer, Application of the two-site Langmuir isotherm to microporous adsorbents, J. Colloid Interface Sci. 92 (1983) 517–524.